Journal of The Electrochemical Society, **150** (3) A316-A325 (2003)
0013-4651/2003/150(3)/A316/10/$7.00 © The Electrochemical Society, Inc.

Mathematical Modeling of Current-Interrupt and Pulse Operation of Valve-Regulated Lead Acid Cells

Venkat Srinivasan,* G. Q. Wang, and C. Y. Wang*,z**

Electrochemical Engine Center and Department of Mechanical and Nuclear Engineering, Pennsylvania State University, University Park, Pennsylvania 16802, USA

Electric and hybrid electric vehicles use valve-regulated lead acid (VRLA) cells that are subjected to dynamic operation with charge, rest, and discharge periods in the order of seconds. Such operation requires more sophisticated models that incorporate the electrochemical double layer. While this effect has been incorporated in a handful of electrochemical systems, the lead-acid cell, with its sluggish reaction kinetics, is one of the few where it is significant. This significance is demonstrated with use of the current-interrupt technique, where the model is used to provide guidelines for the estimation of various resistances. The usefulness of the modeling approach is exemplified by its ability to explore the effect of changing electrochemical area and concentration with state of charge, and the role of parasitic side reactions in the voltage response of the cell. Simulations of pulse charging and dynamic stress test of VRLA cells, where considerable differences are shown when including the double layer, illustrate the need for modifying the presently used modeling approach. In addition, simulations are compared to current-interrupt experiments on commercial cells in order to evaluate the applicability of the model and to identify the differences.
 [DOI: 10.1149/1.1541005]

Manuscript submitted November 15, 2001; revised manuscript received August 21, 2002. Available electronically February 5, 2003.

With renewed interest in the development of electric and hybrid electric vehicles over the last decade, advanced batteries have received much attention. At present, only the valve-regulated lead acid (VRLA) and the nickel-metal hydride (Ni-MH) battery are being actively considered for these applications, while Li-ion cells could become more popular in the future when all safety-related issues are resolved. Of the two candidate battery systems, the low cost and ease of operation of the VRLA battery assures it a prominent role in the years to come. This can be seen from the choice of the VRLA battery as the main power source in a number of electric vehicles (EVs) and as a high power source used in conjunction with an internal combustion engine in hybrid electric vehicles (HEVs).

This renewed interest has spurred research in this area, with focus on improving the performance of the system and tailoring the manufacturing process to achieve the requisite power and energy demands. In particular, the ability of the battery to handle the simplified federal urban driving schedule (SFUDS) and the dynamic stress test (DST)[1] are being extensively studied, as they provide a suitable yardstick to characterize the performance of EV batteries. These schedules, which involve repeated discharge, rest, and charge periods, each lasting a few seconds, test the dynamic response of the system. In addition, recent evidence that the cycle life of the VRLA battery can be extended considerably by the use of smart charging algorithms[2] has spurred interest in current interrupt (CI),[3] pulse, and "burp" (*i.e.*, where a short discharge pulse is incorporated during a pulse charge process) charging of the battery.[4]

While considerable effort has gone into testing batteries under these schemes, a cost-effective method of characterizing them is the use of mathematical models that describe the operation of the cell. Not only is this approach advantageous in reducing the time required to test batteries of different design, it also provides a means of understanding the underlying phenomena that govern its response. While numerous models exist that provide a macrohomogeneous approach to describe the system (for example, see, Ref. 5-10), not enough research has been undertaken in extending the response of the models during dynamic operation of the cell prescribed for EV applications.[11] These applications have pulses and rest periods in the order of seconds, where phenomena with small time constants, specifically double-layer charging, become important, requiring modifications to the existing models.

In addition, the CI technique, frequently used to estimate the various resistances in electrochemical cells,[12] can be simulated only by the incorporation of the double-layer capacitance. When the constant current is interrupted, although the external current is zero, the double layer remained charged, resulting in local currents in the porous electrodes. These currents are caused by the discharging of the double layer onto the electrochemical reaction, which results in the potential changing to reach its equilibrium value with a finite time constant. This time constant can be estimated by equating the double-layer charging current to the current going to the faradaic reaction. Using linear kinetics, this can be approximated to be[13]

$$\tau_{\mathrm{Rct}} = \frac{RTC}{Fi_{\mathrm{o}}} \qquad [1]$$

where the symbols are defined in the notation section. Equation 1 shows that the time constant for the process changes linearly with the specific capacitance (C) and inversely with the exchange current density (i_{o}). In other words, reactions that are kinetically sluggish would result in a large time constant, while those that are facile would have a smaller time constant. For example, the zinc electrode has facile kinetics with i_0 in the order of 10^{-2} A/cm^2,[14] which leads to a value of τ in the order of 50 μs, using a value of double-layer capacitance of 20 μF/cm^2 at room temperature, while the nickel hydroxide electrode, with an i_{o} of 10^{-4} A/cm^2,[15] leads to τ of 5 ms. This small time constant has been the reason the phenomenon has been largely ignored in most mathematical models for batteries. Interestingly, the kinetics of the lead dioxide reaction is very sluggish with i_{o} on the order of 10^{-7} A/cm^2,[5] leading to time constants on the order of seconds, suggesting that this phenomenon could be extremely important under dynamic operation.

Very few studies exist that incorporate double-layer capacitance in the mathematical models for battery systems. Recently Ong and Newman[16] studied the effect of double-layer capacitance in the Li-ion cell, where they analyzed the time constant of the process and the differences in the potential change with and without this effect. Subsequently, this model was extended by Doyle *et al.*[17] to predict the impedance response of the cell, where incorporation of this effect is crucial. Another study by Lin *et al.*[18] focused on the incorporation of a faradaic reaction in the model for an electrochemical double-layer capacitor (EDLC). The authors modeled the behavior of a high-surface-area carbon electrode on which ruthenium oxide was deposited and showed the advantages of using a faradaic capacitor over an EDLC. In addition, while numerous papers study the CI experiment in planar electrodes (*e.g.*, see Ref. 12 and 19), porous electrodes, especially batteries, have been largely neglected. One of the few papers that have analyzed the CI technique in porous elec-

* Electrochemical Society Active Member.
** Electrochemical Society Student Member.
z E-mail: cxw31@psu.edu

trodes is one by Lagergren *et al.*,[20] who modeled the behavior of a molten carbonate fuel cell.

The purpose of this communication is threefold: (*i*) to point out the importance of incorporating the double layer in mathematical models for the lead-acid cell during various dynamic operations, (*ii*) to provide insight into the various physicochemical processes during a CI experiment, and (*iii*) to provide guidelines for estimating the various resistances in the cell from experimental data. The paper first details the mathematical model, after which the importance of the double-layer charging and various underlying phenomena are explored by simulating the CI response of the cell. Subsequently, two examples of dynamic operation are provided, namely, the DST and burp charging, where the importance of including this effect is clearly seen. Finally, experimental data on the CI response of a lead-acid cell is used to gauge the applicability of the model and to provide insight into the differences.

Mathematical Model Development

The VRLA cell modeled in this study is based on previously published models.[10] The cell consists of a lead dioxide positive electrode, a separator, and a lead negative electrode. All three regions are porous and filled with sulfuric acid. The active material is pasted on a conductive lead grid. During charge, while in the positive electrode, lead sulfate is oxidized to lead dioxide according to

$$PbSO_4 + 2H_2O \underset{\text{discharge}}{\overset{\text{charge}}{\rightleftarrows}} PbO_2 + HSO_4^- + 3H^+ + 2e^- \quad E^0 = 1.63 \text{ V } \textit{vs.} \text{ SHE} \qquad [2]$$

In the negative electrode the lead sulfate is reduced to lead according to

$$PbSO_4 + H^+ + 2e^- \underset{\text{discharge}}{\overset{\text{charge}}{\rightleftarrows}} Pb + HSO_4^- \quad E^0 = -0.30 \text{ V } \textit{vs.} \text{ SHE} \qquad [3]$$

$PbSO_4$ is an insulator[21] and Reactions 2 and 3 are thought to occur by the dissolution of $PbSO_4$ into solution as Pb^{2+} ions, which then react electrochemically to form PbO_2 or Pb. In addition to these main reactions, side reactions corresponding to oxygen evolution in the positive electrode according to

$$2H_2O \rightarrow O_2 + 4H^+ + 4e^- \quad E^0 = 1.229 \text{ V } \textit{vs.} \text{ SHE} \qquad [4]$$

and hydrogen evolution in the negative plate according to

$$2H^+ + 2e^- \rightarrow H_2 \quad E^0 = 0 \text{ V } \textit{vs.} \text{ SHE} \qquad [5]$$

also occur. Although the equilibrium potentials of both Reactions 4 and 5 suggest that they occur during normal battery operation, the kinetics of the reactions are sluggish. While oxygen evolution is unavoidable under high state of charge (SOC), the hydrogen evolution reaction (HER) occurs only during extreme overcharge. In addition to Reaction 5, the oxygen reduction reaction, according to

$$O_2 + 4H^+ + 4e^- \rightarrow 2H_2O \quad E^0 = 1.229 \text{ V } \textit{vs.} \text{ SHE} \qquad [6]$$

occurs on the negative electrode, typically during overcharge, due to the large overpotential for the reaction.

The one-dimensional mathematical model used in this paper is based on charge and mass balances derived from first principles. The model equations are similar to the one described previously[10] and are thus not repeated in this paper. Instead, only the charge balance equations, which need to be modified, are described. The following assumptions are made in developing the model: (*i*) the cell is assumed to be isothermal; (*ii*) the mass and charge balance in the electrodes are described using porous electrode theory, where the microscopic details of the pore structure are neglected; (*iii*) the sulfuric acid is assumed to dissociate completely into H^+ and HSO_4^-; (*iv*) formation of Pb^{2+} ions and possible transport limitations are neglected; (*v*) the electrochemically active surface area is assumed to be the area covered by PbO_2 and Pb, and $PbSO_4$ is assumed to be nonconducting; (*vi*) specific adsorption of ions at the electrode surface is neglected, *i.e.*, the mass balances are not altered by the incorporation of the double layer; and (*vii*) the capacitance is assumed to be a constant with SOC (or potential). In addition, the model incorporates the transport of the gas-phase species, which require addition assumptions. However, for all the graphs in the paper, recombination is not important and hence this is not detailed here. For details on the effect of the gassing reactions see Gu *et al.*[22]

Due to assumption (*vi*), the incorporation of the double layer affects the charge balance equations alone. In the matrix phase, the charge balance becomes[16,23]

$$\nabla \cdot (\sigma^{\text{eff}} \nabla \phi_s) - S_e^c - a_{dl} C \frac{\partial(\phi_s - \phi_e)}{\partial t} = 0 \qquad [7]$$

where the source/sink term in Eq. 7, S_e^c, depends on the electrode. In the positive electrode, this is the sum of the reaction currents to the PbO_2 and the oxygen reactions. In other words

$$S_e^c = a_2 i_{n^2} + a_4 i_{n^4} \qquad [8]$$

where the numbers in the subscript correspond to one of the reactions 2-6. In the negative electrode, the Pb, hydrogen evolution, and oxygen reduction reactions occur. Therefore, S_e^c is expressed as

$$S_e^c = a_3 i_{n^3} + a_5 i_{n^5} + a_6 i_{n^6} \qquad [9]$$

As mentioned earlier, the electroactive area corresponds to that of PbO_2 [see assumption (*vi*)] and hence the area changes with SOC and depends on whether the battery is charged or discharged. For the primary reactions (Reactions 2 and 3) this can be expressed as[10]

$$a_j = a_{\max,j}(1 - \text{EUC}^{\xi}) \quad j = 2,3 \quad \text{for discharge} \qquad [10]$$

and

$$a_j = a_{\max,j}\text{EUC}^{\xi} \quad j = 2,3 \quad \text{for charge} \qquad [11]$$

where EUC is the local electrode utilization (estimated using Faraday's law and the maximum capacity of the electrode), $a_{\max}$ the maximum specific surface area of the electrode under consideration, and ξ the morphology correction factor (taken to be 0.6 in this study). In a completely charged cell, EUC is equal to 0.0, while in the discharged state this value is 0.2 in the PbO_2 and 0.27 in the Pb electrode for the dimensions of the electrodes chosen in this study. For the secondary reactions and for the double-layer formation, the specific surface area is calculated from

$$a_j = a_{\max,j}(1 - \text{EUC}^{\xi}) \quad j = 4\text{-}6,\text{dl} \qquad [12]$$

where $a_{\max,4} = a_{\max,2}$ and $a_{\max,5} = a_{\max,6} = a_{\max,3}$. In other words, the area for the main reaction corresponds to the area of the reactants, which changes with SOC, while, the area for the side reaction is that due to the PbO_2 and Pb. This assumption is made because $PbSO_4$ is thought to be an insulator and hence no direct electrochemical reaction is assumed to occur on its surface. Notice that in order to be consistent with the assumption that $PbSO_4$ is an insulator, Eq. 12 assumes that the double layer forms only on the PbO_2 and Pb surface. If the double layer forms on both surfaces in a similar manner, then this surface area would be the maximum surface area at all SOCs. However, this change does not effect the qualitative results presented in this paper and hence is not explored further. Note that if the area for double-layer formation changes with time, the area term would be in the partial differential equation in Eq. 7 (and Eq. 13). However, as the change in area is negligible in the time step used, the value is assumed to be a constant equal to the value in the previous time step.

Similar to Eq. 7, the charge balance in solution can be expressed as

$$\nabla \cdot (\kappa^{\text{eff}} \nabla \phi_e) + \nabla \cdot \left(\frac{RT\kappa^{\text{eff}}}{F} (2t_+^0 - 1) \nabla (\ln c^{H^+}) \right) + S_e^c + a_{dl} C \frac{\partial (\phi_s - \phi_e)}{\partial t} = 0 \quad [13]$$

where σ^{eff} and κ^{eff} are the effective conductivities of the electrode and electrolyte, respectively, which are estimated from the conductivity of the free medium and the porosity based on the Bruggeman correction.[24] This correction is also used to correct the acid diffusion coefficient. The conductivity of the solution and the diffusion coefficient were estimated based on the correlation by Tiedemann and Newman.[5] The currents in Eq. 8 and 9 are expressed in terms of the overpotential and concentration using a kinetic expression. For the primary reactions (Reactions 2 and 3) this is expressed using the Butler-Volmer equation as

$$i_{nj} = i_{oj,ref} \left(\frac{c^{H^+}}{c_{ref}^{H^+}} \right)^{\gamma_j} \left[\exp\left(\frac{\alpha_{aj} F}{RT} \sigma_j \right) - \exp\left(-\frac{\alpha_{cj} F}{RT} \eta_j \right) \right] \quad j = 2,3 \quad [14]$$

while for the oxygen reactions (Reactions 4 and 6) this is expressed as

$$i_{nj} = i_{oj,ref} \left(\frac{c^{H^+}}{c_{ref}^{H^+}} \right)^{\gamma_j} \left[\exp\left(\frac{\alpha_{aj} F}{RT} \eta_j \right) - \left(\frac{c_e^{O_2}}{c_{e,ref}^{O_2}} \right)^{\delta_j} \exp\left(-\frac{\alpha_{cj} F}{RT} \eta_j \right) \right] \quad j = 4,6 \quad [15]$$

For the HER (Reaction 5), the surface overpotential for the reaction is large, and hence the Tafel expression is used

$$i_{nj} = -i_{oj,ref} \left(\frac{c^{H^+}}{c_{ref}^{H^+}} \right)^{\gamma_j} \exp\left(-\frac{\alpha_{cj} F}{RT} \eta_j \right) \quad j = 5 \quad [16]$$

The concentrations in Eq. 14-16 are estimated based on the mass balance expressions. The overpotential, η_j, is evaluated from

$$\eta_j = \phi_s - \phi_e - U_j \quad [17]$$

While the open-circuit potential (OCP, U_j) is given in Table II for the Pb, O_2, and H_2 reactions, the value for the PbO_2 reaction is a function of the acid concentration as given by Bode.[21] The double-layer current is calculated using

$$i_{dl} = a_{dl} C \frac{\partial (\phi_s - \phi_e)}{\partial t} \quad [18]$$

Equations 7 and 13 are the only two equations that are modified in the present model in order to predict the effect of the double-layer capacitance in the cell. For more details on the other model equations, see Ref. 10 and 11.

Numerical Procedure

The resulting equations were solved using a computation fluid dynamics (CFD) technique. The equations are discretized using the control-volume based-finite difference technique introduced by Patankar.[25] The resulting set of algebraic equations were solved iteratively and convergence is considered to be achieved when the relative error between iterations is less than 10^{-6}. All simulations presented in this paper were generated using 29 nonuniform grids in the *x* direction and time steps in the range of 5-500 ms. A typical discharge curve for the cell, lasting tens of hours, is completed in approximately 2 min of central processing unit (CPU) time.

Table I. Cell specific parameters used in generating Fig. 1-10. The top table shows parameters that are generic for the whole cell, while the bottom table shows those that vary for the different sections.

Parameter	Value
Battery weight (kg)	19.3
Width of the electrode (cm)	10.16
Height of the electrode (cm)	12.7
Acid concentration in fully charged state (mol/cm^3)	5.65×10^{-3}

Parameter	Positive electrode	Separator	Negative electrode
Thickness, L (cm)	0.1145	0.1146	0.0785
Porosity in the fully charged state	0.53	0.92	0.57
Saturation level (%)	85	93	85
Matrix conductivity, σ (Ω^{-1} cm^{-1})	5×10^2	-	4.8×10^4
Specific interfacial area, a_j	230000	-	23000
Morphology correction factor, ξ	0.6	-	0.6

Results and Discussion

Current-interrupt.—We begin this section by analyzing the effect of adding the double-layer capacitance into the model, and gauging the effect of the various parameters on the time constant during a CI. All the plots in this paper were generated on a VRLA battery of nominal capacity 70 Ah, which consists of 26 cells in parallel and four cells in series. The dimensions of the plates and other essential features of the battery are listed in Table I and are based on the design of a commercial cell used for EV applications. The various equilibrium, kinetic, and transport properties used are listed in Table II, which are reproduced from Ref. 22. Unless specified, all the plots were generated for a constant current of 25 A impressed on the whole battery, after which the current is interrupted. Profiles will be shown for a single cell in the battery (capacity 2.69 Ah), corresponding to a current of 0.961 A.

Figure 1 shows the potential profile when the cell at rest at 50% SOC, wherein the concentration profiles are uniform, is subjected to a 15 s discharge after which the current is interrupted. The SOC is referenced to this nominal capacity of the battery (70 Ah) and is considerably smaller than the true theoretical capacity based on the amount of active material or the amount of acid. Therefore, 50% SOC corresponds to the acid concentration and the active material loading when the battery is discharged by 35 Ah. The figure plots the potential profiles without the double-layer (·····) and four profiles with double-layer capacitance, corresponding to: (*i*) the values of the parameters as listed in Table II (——); (*ii*) with the diffusion coefficient of H_2SO_4 close to infinity (----); (*iii*) the value of i_o of reaction 2 ten times the value in Table II (–···–); and (*iv*) the value of i_o of reaction 3 ten times that in Table II (–·–). Note that in plots (*ii*)-(*iv*), all other parameter values other than the one changed were kept the same as that in Table II.

Comparison between the curves with and without the double layer clearly shows the importance of incorporating the effect. The time required for the profile to reach a steady state, seen to be in the order of 5 s in Fig. 1, asserts to the importance of incorporating this effect under such dynamic operations. When the diffusion coefficient of the acid is increased, so as to eliminate any diffusion limitation in the cell, a plot very similar to the previous case is seen. Although the two plots start to deviate after 2 s on open circuit, the differences are minimal and correspond to approximately 0.1-0.2 mV, with the potential of the cell with larger diffusion coefficient being higher. In a lead-acid cell, the OCP is related to the acid concentration, and hence any differences in the concentration between different points in the cell result in changes in potential. At very long times (approximately 20 min) all the curves collapse,

Table II. Equilibrium, kinetic, and transport parameters used to generate the various plots in the figures. The parameters were taken to be the same as those in Ref. 22.

Parameter	Value
Reference acid concentration $c_{ref}^{H^+}$ (mol/cm^3)	5.65×10^{-3}
Reference concentration of oxygen in electrolyte, $c_{e,ref}^{O_2}$ (mol/cm^3)	1×10^{-3}
Transference number of H^+	0.72
Specific capacitance, C (μF/cm^2)	20
PbO_2/$PbSO_4$ reaction	
Exchange current density $i_{o2,ref}$ (A/cm^2)	4×10^{-7}
Exponent of acid concentration dependence, γ	0.3
Anodic transfer coefficient, α_{a2}	1.21
Cathodic transfer coefficient, α_{c2}	0.79
Pb/$PbSO_4$ reaction	
Exchange current density, $i_{o3,ref}$ (A/cm^2)	4.96×10^{-6}
Exponent of acid concentration dependence, γ_2	0
Anodic transfer coefficient, α_{a3}	1.55
Cathodic transfer coefficient, α_{c3}	0.45
Oxygen generation reaction	
Exchange current density, $i_{o4,ref}$ (A/cm^2)	2.5×10^{-27}
Exponent of acid concentration dependence, δ_4	0
Anodic transfer coefficient, α_{a4}	2
Cathodic transfer coefficient, α_{c4}	2
OCP *vs.* Pb reaction, U_4, U_6 (V)	1.649
Hydrogen evolution reaction	
Exchange current density, $i_{o5,ref}$ (A/cm^2)	1.56×10^{-15}
Exponent of acid concentration dependence, γ_4	1
Cathodic transfer coefficient, α_{c5}	0.5
OCP *vs.* Pb reaction, U_5 (V)	0.356
Oxygen recombination reaction	
Exchange current density, $i_{o6,ref}$ (A/cm^2)	2.5×10^{-36}
Exponent of acid concentration dependence, δ_6	0
Anodic transfer coefficient, α_{a6}	2
Cathodic transfer coefficient, α_{a6}	2
OCP *vs.* Pb reaction, U_6 (V)	1.649

suggesting that the cell has reached a steady state. The figure shows that although a long time is required for the concentration to equilibrate, the differences in potential are minimal. This small change occurs because of the short discharge time (15 s) before interruption wherein the concentration gradients do not build up significantly. If the concentration gradients were allowed to build, then a greater voltage drop is expected. In a lead-acid cell, as the voltage is based on the acid concentration, these gradients would result in coupling with reactions which would occur at different rates at different parts of the porous electrodes, making interpretation difficult. In this paper, we have tried to minimize this effect in order to concentrate on the effect of the double layer.

The negligible effect of acid diffusion is further asserted when the exchange current density for Reaction 2 is made ten times larger. The time constant for the process decreases by an order of magnitude, as seen in the figure. Note that this is consistent with Eq. 1, suggesting that the time constant seen is indeed the effect of the reaction resistance. Further, when the exchange current density of Reaction 3 is increased instead of the positive electrode, no differences are seen in the time constant. This is consistent with the fact that the exchange current density of Reaction 3 is larger than that of Reaction 2 by an order of magnitude, hence making this electrode insignificant in the behavior of the cell. Note that both these curves result in a significant decrease in the potential on passing a current: a result of the decrease in the kinetic polarization losses with increasing exchange current density. In summary, Fig. 1 shows that the main cause for the time constant associated with a CI in a lead-acid cell is the exchange current density of Reaction 2. While concentration gradients take a considerably longer time to dissipate, its effect

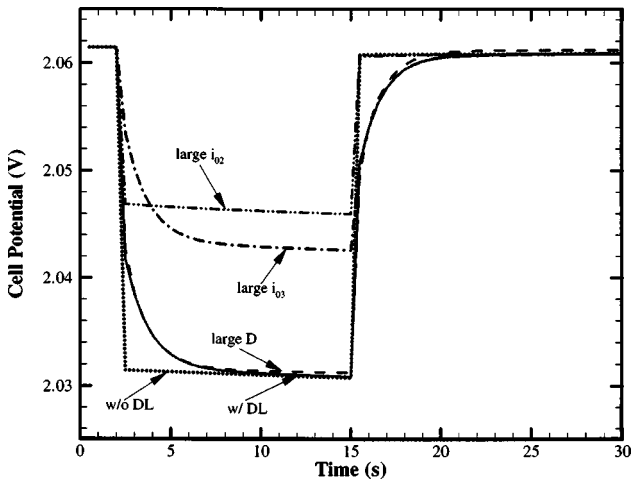

Figure 1. Potential *vs.* time for a 70 Ah VRLA cell when subjected to a constant current of 0.961 A per cell for 15 s, after which the current is interrupted at 50% SOC. The plot shows the curves (·····) without the double layer, and four sets of curves (——) with double-layer corresponding to the parameters in Table II, (– – –) with large D_{H+}, (–·–) with large i_{o2}, and (–·–) with large i_{o3}.

on the cell potential is negligible under the conditions simulated in this paper.

Figure 1 has often been used as a method of estimating the various resistances in a cell by measuring the potential drops after suitable time intervals.[12] We now examine the nature of the curve more closely in order to estimate the time for each process to dissipate. Figure 2a shows the solution potential and 2b the currents resulting from the double layer and the primary reactions across the cell at 50% SOC. At this SOC, the currents to the secondary reactions are negligible and hence are not shown in the figure.

Prior to interruption, the potential of the cell does not change appreciably, as seen in Fig. 1, and hence the double-layer current is negligible in both electrodes (see Fig. 2b). In addition, although there is an appreciable change in the overpotential profile in the porous electrodes (not shown), the current to the primary reactions are uniform; a consequence of the sluggish kinetics of the reactions. The existence of the external current results in a considerable potential drop across the cell, as seen from the liquid phase potential profile, with a greater drop in the positive electrode compared to the negative, as a result of the differences in their thickness.

At the instant the current is interrupted, current transfer from the electrode to the separator region is halted. As no current flows through the separator region, the potential drop goes to zero, as seen from the solid line in Fig. 2a. However, in the porous electrode, the double layer remains charged and hence, the overpotential for reaction is maintained (reflected in the reaction currents in Fig. 2b). This overpotential results in the transfer of current from the matrix to the solution and consequently results in potential drops in the solution phase, all of which remain unchanged on interruption. However, as the current transferred from the electrode to the separator goes to zero, the solution potential (related to the current through Ohm's law) changes at this interface so as to make the flux zero, as seen from the solid line in Fig. 2a. As the solution potential changes in this region, the double-layer current, related to the time change of this quantity, changes dramatically, as seen from the large current at this interface in Fig. 2b. If the simulations were conducted with a infinitesimally small time step, then this profile would be a delta function with the peak at the electrode/separator interface. The double-layer profile in Fig. 2b is similar to the short-term behavior of an EDLC when subjected to a constant current[18,26,27] and corresponds to a case when the matrix conductivity is large compared to the solution. This similarity would extend to the case where the solution conductivity is large compared to the matrix, where the

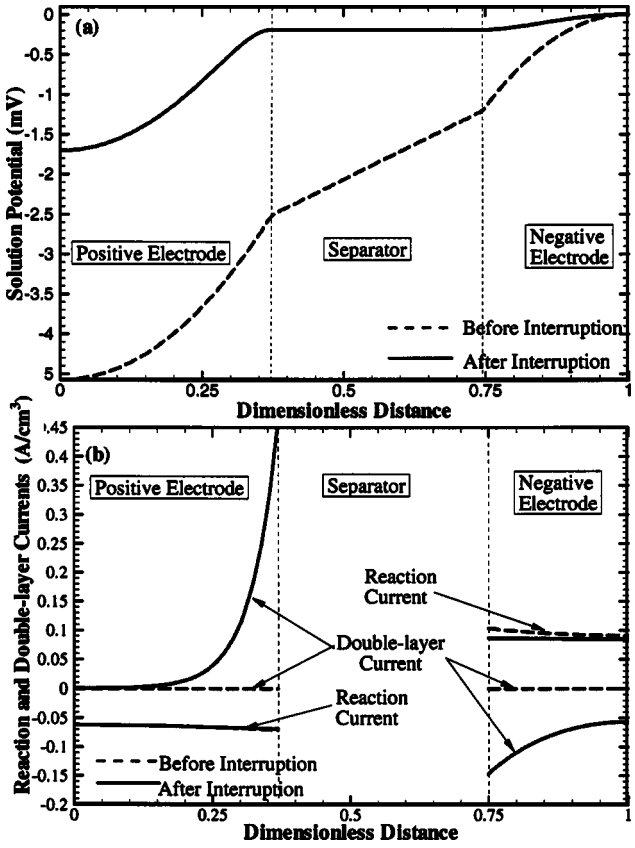

Figure 2. (a) Solution potential, and (b) double-layer current and reaction current distributions across the cell 2 ms (– – – –) prior to and (——) after interruption, at 50% SOC. Currents in the separator are zero and are not shown in the figure. The conditions are the same as those corresponding to the solid line in Fig. 1.

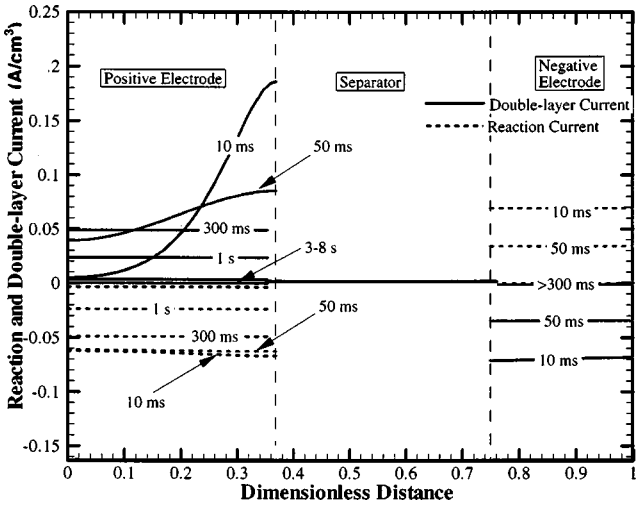

Figure 3. (——) Double-layer and (– – – –) reaction current after the interruption of the current in a VRLA cell. The plot shows profiles after the point in time represented in Fig. 2.

double-layer profile would be the mirror image of the one in Fig. 2b. For comparable values for the two, the double-layer current is large in the two ends of the electrode and smaller in the center.

In other words, at the instant of interruption, for the case when the matrix conductivity is very large compared to the solution, only the region at the electrode/separator interface experiences changes, with the solution potential, solution current, and overpotential remaining unchanged, prior to and after interruption, in the rest of the porous electrodes. Therefore, the potential drop at this instant is solely due to the resistance of the separator.[20] This is similar to a high-frequency impedance experiment where the resistance measured corresponds to the separator resistance (for the case when the matrix phase conductivity is large compared to the solution). However, while in the impedance experiment this is a consequence of the current taking the path of least resistance across the cell; in a CI, this is a consequence of the double layer sustaining the overpotential at all points in the porous electrode upon interruption.

However, one difference between the double-layer current profile of an EDLC and that in Fig. 2b is in the flux of this quantity at the electrode/separator region. In an EDLC this flux is equal to zero, while in Fig. 2b this is finite. Simplistically, for a case where the matrix potential is invariant, the flux of the double-layer current is the time change in the flux of the solution potential. In an EDLC, the flux of the solution potential is a constant (corresponding to the current) during a constant current operation, and hence this quantity is zero. However, in Fig. 2b the flux of the solution potential changes from being constant prior to interruption (equal to the constant current) to zero after interruption. This results in a finite flux of the double-layer current at this surface.

However, as the interruption is continued, the lead-acid cell imitates the behavior of an EDLC, as shown in Fig. 3, where the double-layer and reaction currents are plotted across the positive electrode as a function of time. This is a result of the flux of the solution potential at the interface remaining unchanged with time (and equal to zero). With time, the double-layer current profile moves into the porous electrode and the currents become more uniform, similar to that in an EDLC.[18,26,27] In addition, the area under the curve (corresponding to the total charge transferred to the double layer) remains fairly constant, which is seen from the comparable reaction currents between the 10 and 50 ms curves in the positive electrode. (Note that on interruption, the total double-layer current equals the reaction current in each electrode.) The nonuniformity of the double-layer charging profile results in passage of current from one part of the porous electrode to another, resulting in ohmic losses. As the profile becomes more uniform, these losses are dissipated. This decrease in ohmic losses results in the sharp drop in potential with time, seen in Fig. 1, on open circuit, after the dissipation of the losses in the separator. As the potential changes dramatically in a short time, the double-layer term in Eq. 7 and 13 dominate over the reaction terms, hence making the governing equations similar to that of an EDLC. Considering this similarity, the time constant for the profile to become uniform can be approximated using the time constant for double-layer charging, namely

$$\tau_{\text{ohmic}} = \frac{aCL^2(\kappa + \sigma)}{\kappa\sigma} \qquad [19]$$

When the dimensionless time, t/τ_{ohmic}, is very small, the double-layer profile is very nonuniform and the potential drop measured by the interrupter technique is that corresponding to the shortest path across the cell (equal to the separator resistance when the matrix conductivity is large). As t/τ_{ohmic} approaches 1.0, the profile becomes more uniform and the value estimated is the sum of the drop across the porous electrodes and the separator. It should be noted that estimating the ohmic drop across the porous electrode is nontrivial as it depends on the exchange current density, solution conductivity, and amount of active material and hence changes with SOC.

After the ohmic losses in the porous electrode are dissipated (approximately 10 ms for the negative and 200 ms in the positive), kinetic losses start to dominate the process. As mentioned earlier, although losses due to concentration variations also occur simultaneously, they play a negligible part in the potential drop in the lead-acid cell. During this time, the charge in the double layer starts

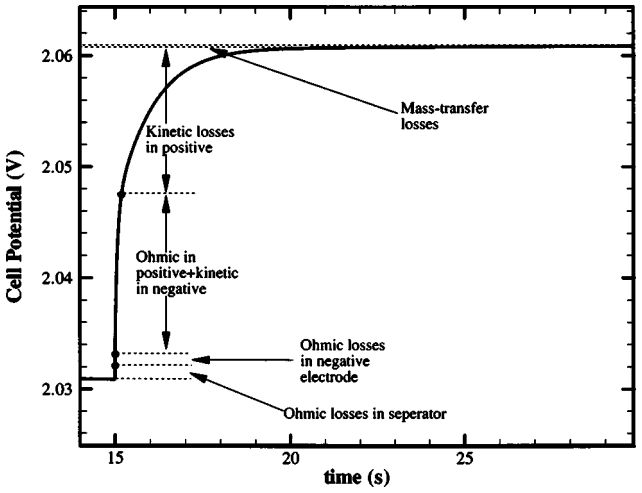

Figure 4. Representation of various regions and the time constant associated with each process during a current interrupt. The time constant represents the end of each process to dissipate. Note that the voltage losses during the time for the ohmic losses in the positive electrode to dissipate are dominated by dissipation of kinetic losses in the negative.

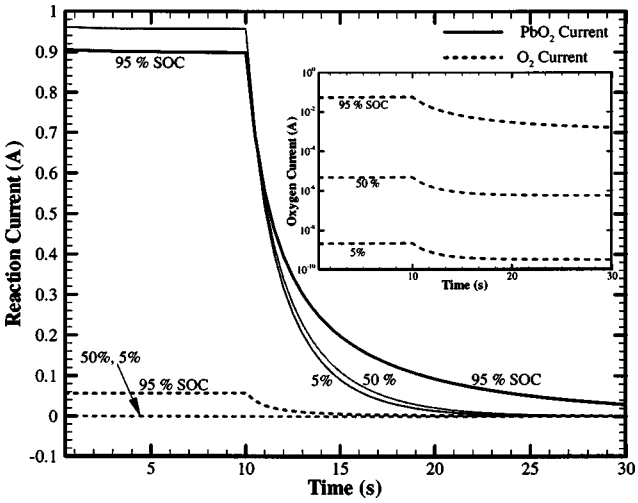

Figure 5. (——) PbO_2 and (– – – –) oxygen evolution currents as a function of time when the current is interrupted from charge at different SOCs. The plot shows the reaction currents integrated over the positive electrode. The inset plot shows the oxygen current in more detail in logarithmic scale.

to dissipate, as seen from the decreasing currents in Fig. 3 after the double-layer profile becomes uniform, and the cell potential starts approaching the open-circuit value. Under these conditions, the double-layer term in Eq. 7 and 13 are negligible. The time constant for this process can be derived from the linearized concentration-dependent Butler-Volmer equation (Eq. 14), analogous to Eq. 1 as

$$\tau_{\mathrm{Rct}} = \frac{RTa_{\mathrm{dl}}C}{Fa_{\mathrm{j}}i_{\mathrm{oj,ref}}\left(\frac{c^{\mathrm{H}^+}}{c^{\mathrm{H}^+}_{\mathrm{ref}}}\right)^{\gamma_{\mathrm{j}}}} \qquad [20]$$

In Eq. 20 the term $a_{\mathrm{dl}}/a_{\mathrm{j}}$ appears as the area for reaction may be different than the area for double-layer formation, caused by the assumption that $PbSO_4$ is nonconducting. During discharge these two quantities are the same, while on charge, they increase with SOC. Substituting the appropriate parameters leads to an estimate of τ_{Rct} in the order of 300 ms for the negative and 2-3 s for the positive. For the behavior considering both the double-layer and the faradaic reaction with linear kinetics in a porous electrode with no concentration variations, see Ong and Newman.[16]

At longer times, the double layer is fully discharged and all internal currents go to zero. However, small changes in the cell potential continue to occur due to the existence of concentration variations across the cell. These can be estimated based on the time constant for mass transfer, namely

$$\tau_{\mathrm{MT}} = \frac{L^2}{D_{\mathrm{H+}}} \qquad [21]$$

where L is the characteristic length over which diffusion occurs. Assuming this value is in the order of the separator thickness (0.1146 cm) provides an estimate of τ_{MT} to be approximately 1300 s for a $D_{\mathrm{H+}}$ of 1×10^{-5} cm^2/s.

In summary, the potential response after a current interrupt in the lead-acid cell can be divided into the different regions shown in Fig. 4. At times close to 0 s, the interrupter technique provides the value of the separator resistance. From 0 s to the time constant approximated by Eq. 19, the profile is dominated by ohmic losses in that negative electrode. Subsequently, both the ohmic losses in the positive and the kinetic losses in the negative dissipate for a time approximated by either Eq. 19 or 20, as both yielded similar values for the cell under study. Subsequently, kinetic losses in the positive electrode dissipate, whose time constant is approximated by Eq. 20. Finally, concentration variations start to dominate the process. Note that the time constant is not an exact measure of the time required to reach a steady state and is meant to provide an order-of-magnitude estimation (*e.g.*, for an exponential function, one time constant corresponds to the time to reach 67% of the steady state). In addition, the regions marked in Fig. 4 indicate the end of a process and do not suggest that no other process occurs in that regime. For example, while the positive electrode is in the ohmic region, the negative electrode is in the kinetic region and represents most of the potential drop. However, considerable insight can be achieved by analyzing the time constants based on the aforementioned approach. Specifically, experimental half-cell voltage, measured with respect to a reference electrode, combined with this model, can be used to isolate each phenomenon separately.

Having established that the main contribution to the time constant for the lead-acid cell is the dissipation of the kinetic resistance in the positive electrode, we now examine the effect in more detail. The effects are shown for the positive electrode, as the negative electrode does not contribute significantly to the time constant after interruption. The equilibrium potential of the oxygen evolution reaction (OER, Reaction 4) is lower than the main reaction (Reaction 2); therefore, both occur simultaneously during charge and discharge. While the main reaction changes sign depending on the direction of the current (oxidation on charge and reduction on discharge), the OER remains the same (oxidation). Therefore, on interruption, the currents to the two reactions and the double layer are distributed differently depending on whether the cell is charged or discharged, as seen in Fig. 5 and 6. Figure 5 shows the PbO_2 and the oxygen currents when the cell is charged for 10 min from rest with a current of 0.961 A, after which the cell is interrupted, for three SOCs. The currents were calculated by integrating the reaction current across the positive electrode. The figure shows three distinct characteristics, namely, (*i*) an increase in the oxygen current with increasing SOC, (*ii*) an asymptotic decay in both currents, once the external current is interrupted, and (*iii*) an increase in the time constant with increasing SOC. As the SOC increases, the overpotential for the OER is larger, which in turn results in a larger current to the side reaction. Once the current is interrupted, this overpotential is maintained; hence, as much as 10% of the total current is transferred to the side reaction. With time, the cell potential decreases, thereby decreasing the overpotential for both the reactions, resulting in a decrease in the reaction currents. This is seen more clearly in the inset plot, where the oxygen current is replotted in logarithmic scale.

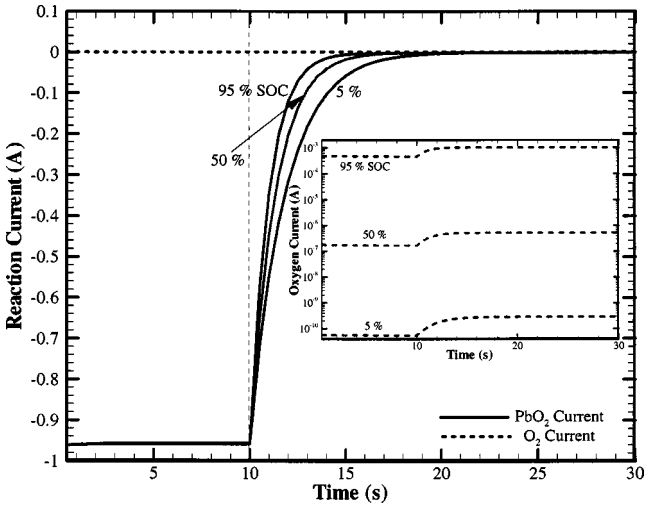

Figure 6. (——) PbO_2 and oxygen evolution (— — —) currents as a function of time when the current is interrupted from discharge at different SOCs. The plot shows the reaction currents integrated over the positive electrode. The inset plot shows the oxygen current in more detail in logarithmic scale.

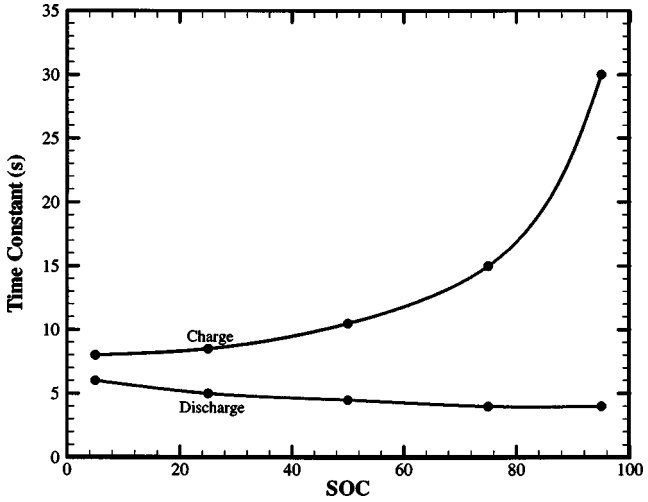

Figure 7. Time constant *vs.* SOC during a CI on charge and discharge. The time constant was estimated using the time at which the slope of the voltage-time curve is less than 1×10^{-4}.

Both the lower currents at lower SOC and the decay after interruption are clearly seen. Note that the steady-state oxygen current is the self-discharge current for the cell at that SOC. As both the PbO_2 current and the oxygen current are positive in Fig. 5, the double-layer current (not shown) is the sum of the two values, on open circuit. In other words, on open circuit, the double layer discharges onto both the main and side reactions, thereby dissipating the charge faster.

The third phenomenon in Fig. 5, namely, the increase in time constant with increasing SOC, can be better understood by analyzing the various terms in Eq. 20. As both the capacitance and the exchange current density are assumed to be a constant with SOC (or potential), the time constant depends on two terms, namely, (*i*) the ratio of the area for double-layer charging and that for electrochemical reaction and (*ii*) the ratio of the acid concentration to the reference acid concentration arising from the concentration dependence of the exchange current density. On charge, with increasing SOC, the PbO_2 surface area increases and consequently, the $PbSO_4$ area decreases. Therefore, the area for double-layer formation (a_{dl}) increases and the area for reaction (a_j) decreases. From Eq. 20 it is clear that this change would result in an increase in the time constant with increasing SOC. However, competing with this effect is the influence of the acid concentration. As the cell is charged, the acid concentration increases and approaches the reference concentration (taken to be 5.65 M in this study). Therefore, the ratio of these quantities increases with SOC. This, in turn, results in a decrease in the time constant with increasing SOC, as seen from Eq. 20. However, the decrease is not enough to offset the large increase due to the increase in surface area. Hence, Fig. 5 shows that on charge, the time constant increases with increasing SOC due to the increase in the area for double-layer formation.

In contrast, during discharge, decreasing the SOC results in an increase in the time constant, as seen from Fig. 6. The graph plots the PbO_2 and the oxygen current when the cell is discharged for 10 min at a current of 0.961 A, after which the current is interrupted, at different SOCs. During discharge, the area for double-layer formation is the same as that for reaction; therefore, the ratio of the two is always 1.0. However, on discharge, the acid concentration decreases, therefore decreasing the ratio of the acid concentration to its reference value. This, in turn, results in an increase in the time constant with decreasing SOC, as seen from Eq. 20. However, note that the increase in this figure is not as pronounced as that seen in Fig. 5, asserting the fact that the concentration change has a smaller effect as compared to the effect of the changing areas.

In addition to the differences in time constants, Fig. 5 and 6 also differ in the distribution of the current on interruption among the three processes. On discharge, the main reaction is negative (reduction), while the OER and the double-layer current (not shown) are positive. Therefore, on open-circuit, oxygen evolution and double-layer charging sustain the main reaction, thereby increasing the time required to dissipate the charge. Note that on interruption, the potential increases, thereby decreasing the overpotential for the main reaction, but increasing the overpotential for the side reaction (seen clearly in the inset plot). With time, the double layer is discharged and the oxygen evolution current reaches a steady state corresponding to the self-discharge current (the same as that in Fig. 5 at a particular SOC). Note that the contribution of the oxygen current is insignificant during both charge and discharge except at high SOCs, as the kinetics for this reaction is poor in the lead-acid cell. Other batteries (*e.g.*, Ni-MH), where the kinetics of this reaction is considerably larger, would show significant effects at high SOCs.

The changes in the time constant seen in Fig. 5 and 6 are summarized in Fig. 7, where this quantity is plotted *vs.* SOC on charge and discharge. For this plot, the time constant was defined as the time at which point the slope of the potential *vs.* time curves, estimated based on a two-point difference formula, is less than 1×10^{-4} V/s. Figure 7 shows two characteristics that were described in Fig. 5 and 6, namely, (*i*) the time constant on charge is greater than that on discharge at all SOCs; (*ii*) the time constant decreases with increasing SOC on discharge, and (*iii*) the time constant increases on increasing SOC on charge. As mentioned earlier, these changes are caused by changes in the area for reaction and double-layer formation and due to changes in the acid concentration as defined in Eq. 20. Note that Fig. 7 would be different if the double layer was assumed to form on both the PbO_2 and the $PbSO_4$ surfaces. Under such conditions, the numerator in Eq. 1 is a constant while the denominator varies. On charge, the surface area decreases with increasing SOC, while the concentration of acid increases. As the acid concentration has a smaller effect compared to the surface area, this results in a decrease in time constant, similar to the case when the double-layer area changes with SOC. On discharge, both the surface area and the acid concentration decreases, which results in an increase in time constant with decreasing SOC, similar to Fig. 7. Hence, qualitatively, Fig. 7 remains the same irrespective of the choice of the area for double-layer formation, although the quantitative values may be different.

Figure 7 suggests that the interrupter technique may provide a means of estimating the change in the electrochemically active sur-

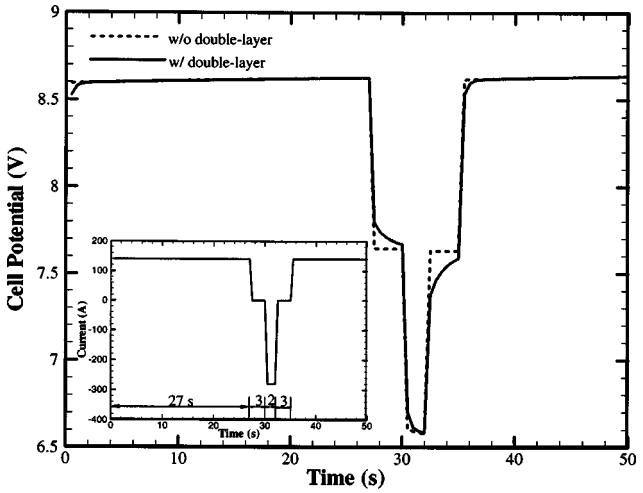

Figure 8. Voltage profile of a VRLA cell when subjected to the burp charging algorithm at 0% SOC. The current profile is shown in the inset. The plot shows the voltage profiles (——) with and (— — —) without the double layer.

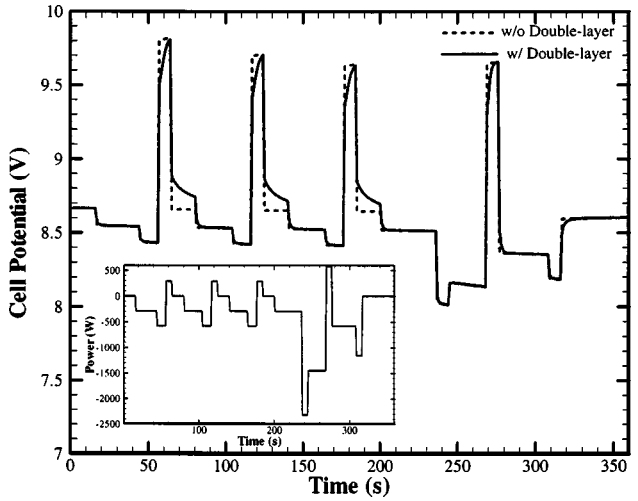

Figure 9. Voltage response of a VRLA cell under the DST. The power that is impressed on the battery is illustrated in the inset plot. The plot shows the voltage profiles (——) with and without (— — —) the double layer.

face area with SOC in lead acid cells. Preliminary experiments on a commercial lead-acid cell show considerable differences in the time constant between different SOCs and between charge and discharge. However, the time constants measured experimentally were an order of magnitude larger than that predicted by the simulation. These differences are explored further in the last section of this paper.

Dynamic operation.—We now examine the effect of adding the double-layer capacitance on dynamic operation of the battery under the burp and DST cycles. Pulse and burp charging of VRLA cells has been initiated as a means of increasing the charging efficiency and cycle life. When lead-acid batteries are charged, acid is produced as seen from Eq. 2 and 3. However, fast charging of cells would result in the nonuniform production of acid across the cell with more produced at the electrode/electrolyte interface. The pulse charging is used to provide time for the equilibration of the acid concentration during the rest periods (*ca.* 3 s). In addition, the time is useful in dissipating the heat generated in the cell.[3] Figure 1 shows that under such operation, the inclusion of the double layer is essential in predicting the resulting potential transients. The burp charging algorithm is an extension of the pulse operation, wherein a discharge pulse is incorporated into a regular CI (see inset in Fig. 8). The discharge pulse results in the consumption of acid, which is thought to help in achieving a more uniform distribution. In addition, the pulse charging has been seen to aid in improving the cycle life of the cells by reducing the sulfation of the negative electrode.[3] However, considerable research is needed in order to understand these effects better.

A recent model of the VRLA cell has attempted to describe the pulse and burp operation of the cell, although the model does not account for the double-layer effect.[4] Figure 8 illustrates the importance of this effect in models describing burp operation. The figure shows the potential profile during one such operation simulated at 0% SOC, with and without the double layer. The short time of rest and discharge results in significant differences in the predicted potential when incorporating this effect. Note that the differences would change as a function of SOC depending on the differences in the area for double-layer charging and reaction and on the acid concentration, as mentioned previously. Note that small differences are also seen when the cell is discharged (or charged) from rest, with the change in potential being more gradual with the inclusion of the double layer, consistent with previous studies on other batteries.[16]

Another commonly used test for EV batteries is the DST algorithm,[1] where the cell is subjected to repeated charge, discharge, and rest operations. The profile can be thought of as a series of constant power experiments. The impressed power is represented as a percentage of the peak power of the cell. The USABC mid-term goal for batteries is a peak power of 120 W/kg, which is assumed to be the value for the battery simulated in this paper. Combined with the weight of the battery (assumed to be 19.3 kg), this yields the impressed power, shown in the inset plot in Fig. 9. Figure 9 also shows the potential profile of the cell simulated with and without the double layer at 100% SOC. Significant differences are seen between the two profiles, especially when the cell current is switched off from either a charge or discharge. In addition, similar to what is seen in Fig. 8, a gradual change in potential is seen when the cell switched from open circuit to an impressed power. In summary, Fig. 8 and 9 demonstrate the importance of including the double-layer effect when modeling lead-acid cells under various dynamic operations.

Comparison of the model to experimental data.—Having demonstrated the need for incorporating the double layer, we examine the ability of the model to predict the experimental potential profile on VRLA batteries on interruption. The experiments were performed on a 85 Ah commercial VRLA cell that has 13 cells in parallel and four cells in series. The cell was first completely charged using a series of constant currents of decreasing amplitude, after which the cell was discharged for 5 min at 92 A and the current interrupted. The resulting cell potential is plotted with time (taken at 10 ms intervals), denoted by the symbols in Fig. 10. In the figure, zero time indicates the point just prior to interruption (corresponding to the closed-circuit potential). Note the large time constant (greater than 50 s) needed for the cell to reach a steady state.

Figure 10 also shows the predictions of the model under these conditions. The values of the various cell specific parameters were kept the same as that in Table II. As the model predicts the behavior of cells with electrode thickness half that of real cells, it was assumed that the battery consists of 26 cells in parallel. The dashed line in Fig. 10 corresponds to the model parameters listed in Table I. The differences between the model and experimental data are substantial and can be divided into (*i*) the inability of the model to predict the closed circuit potential; (*ii*) the inability to predict the large time constant on interruption; and (*iii*) the inability to predict the potential at long times. The inability to predict the potential at long times could be caused by an underestimation of the initial acid concentration in the cell. The inability to predict the closed circuit potential could be caused by added kinetic, ohmic, or mass-transfer polarization than that predicted in the model. Considering the differences in the time constant also, it was thought that the value of a_j

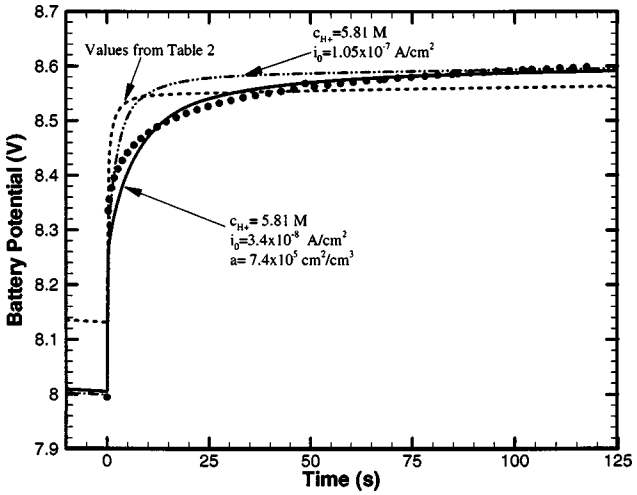

Figure 10. Comparison of the model (lines) to experimental CI data (symbols) generated on a 85 Ah commercial VRLA cell. The curves show the model predictions (— — —) with the values in Table II, (–···–) with i_{o2} and c_{H+} adjusted, and (——) a_{max} also adjusted in order to fit the data. 0 s represents time just prior to open circuit.

and/or i_o could be different than that presently used in the model. An increase of the acid concentration from 5.65 to 5.81 M and a decrease in the i_o from 4 to 1.05×10^{-7} A/cm^2 yielded an adequate fit to the closed-circuit potential and to the potential at long times (dashed-dotted line).

It is conceivable that the exchange current density is actually smaller than that in Table II as considerable differences appear to exist in the literature on the values of the exchange current density and surface area. The values for these quantities in Table II were based on the paper by Newman and Tiedemann, which results in the value of ai_o of ~0.1 A cm^3.[9] The value of ai_o is very similar to the value previously reported by Tiedemann and Newman,[5] where the authors separate the two quantities by measuring the surface area based on the Brunauer-Emmett-Teller (BET) technique, from which the i_o was reported to be 6×10^{-7}A/cm^2. In addition, these values were found to describe the voltage response at different currents adequately. Values of ai_o in the same range have been used by other authors (*e.g.*, see Nguyen and White[7]) with a much smaller surface area and consequently a larger i_o. While only the value of ai_o is important in predicting the potential drop with increasing rates due to kinetics in a porous electrode, the present study requires an accurate estimate of each of these quantities. It should be noted that there are reports in the literature of considerable higher exchange current densities for the reaction. For example, LaFollette and Bennion[28] use a value of 1.78 mA/cm^2, while Guo *et al.*[29] and Carr and Hampson[30] use 0.32 mA/cm^2, all three authors suggesting that the electrode reaction is facile. The latter value appears to have originated from a paper by Aguf,[31] where the exchange current density of this reaction was measured using impedance spectroscopy. However, as the author himself notes, the value is reported with respect to the apparent area of the electrode and not the true surface area. Significant differences could exist between these two values, as noted by the author. Therefore, considering the uncertainty in this value, the smaller value is thought to be plausible.

Even if the decrease in i_o is acceptable, the time constant predicted by the model is an order of magnitude smaller than that observed experimentally. Although the new parameters show a small increase in the time constant, the differences with the data are considerable. This slight increase in the time constant is a consequence of the decrease in i_o as predicted by Eq. 20. An even smaller value of i_o would result in much better fits to the open-circuit data; however, the closed-circuit potential predicted would be considerably lower than that shown experimentally. The surface area has no effect on the time constant, as, on discharge, the area for double-layer formation is same as that for reaction. However, the effect of a_j is same as that of i_o in predicting the closed-circuit potential of the cell as dictated by the Butler-Volmer equation (Eq. 14). Therefore, the i_o was decreased in order to fit the time constant and a_j increased correspondingly to fit the closed-circuit potential. Infinite combinations of the two, with ai_o kept constant at 0.025 A/cm^3, can be used to generate the model plots. Using i_o of 3.4×10^{-8} A/cm^2 and a_{max} of 7.4×10^5 cm^2/cm^3 (instead of 2.3×10^5 cm^2/cm^3) yielded the best visual fit to the data. Note that this value of i_o is an order of magnitude lower than that reported previously. More experimentation is needed to see if such a low value is acceptable.

However, even under these conditions, some variations are seen between the model and the data. Efforts to change the parameters to make the fit better were unsuccessful. It would appear that the model underpredicts the importance of mass transfer when compared to the experiment. However, the diffusion of acid does not appear to provide much change in potential when the cell is only discharged for a short time, as mentioned earlier, and a considerably lower diffusion coefficient would be needed in order to make the fits better. It is possible that other rate-limiting effects (*e.g.*, diffusion of Pb^{2+} ions) also contribute to the potential profile shown in Fig. 10, although their contribution appears to be of less importance than the discharging of the double layer. In addition, the potential dip effect, thought to be a consequence of nucleation of $PbSO_4$ crystals, could also contribute to the data shown in Fig. 10. Finally, as the experimental data was conducted on cell stacks, there is a possibility of differences in concentration between cells giving rise to varying voltage changes during interruption between the various cells, thereby causing the differences seen between the model and the experiments. However, the short discharge time before interruption (5 min) is small enough not to cause an appreciable change in concentration; hence, this effect is expected to be minimal. However, the small differences that are still seen in Fig. 10 may well be caused by this effect.

Inclusion of one or all of these effects may yield better fits to the data. Considering that detailed information on the cell parameters are not adequate, extensive model-to-experimental comparisons at different SOCs may not be meaningful. Controlled experiments, where quantities like the electrode and separator thickness and porosity, concentration of acid, surface area, etc., are all known, would provide a better means of making this comparison.

Conclusions

This paper details the development of a mathematical model for a VRLA cell with the aim of simulating the operation under dynamic response typically used to test EV and HEV batteries. These tests have charge, discharge, and rest periods in the order of seconds that require the incorporation of the electrochemical double layer in the existing cell models. The paper shows that the sluggish kinetics of the lead-oxide reaction results in time constants in the order of seconds when the cell is subjected to a current interrupt, thereby providing an explanation for this experimental observation. Incorporation of the double layer allows us to understand the interrupter technique in detail, with the aim of providing guidelines for estimating the various cell resistances. The technique was seen to have similarities to electrochemical double-layer capacitors under short times. The time constant of the VRLA cell was seen to be dictated by the kinetics of the positive electrode and seen to change with SOC. These changes were explained by analyzing the current transferred to the main and side reactions and by studying the effect of changes in the electrochemical area and concentration with SOC. While the changes in concentration (with resulting changes in the exchange current density) were seen to effect the time constant on discharge, the change in area was seen to dominate the effect on charge. Owing to the poor kinetics for the side reactions, little effect was seen except under high SOCs.

Simulation of the dynamic stress test and burp operation (*i.e.*, where a short discharge pulse is incorporated during a pulse charge process) were used to demonstrate the importance of modifying existing models for the cell when simulating EV or HEV batteries. Finally, experimental data was used to gauge the applicability of the model and to provide insight into the differences. The presently used kinetic parameters were seen to be inadequate in explaining both the closed-circuit potential and the time constant for the reaction. A decrease in the exchange current density by an order of magnitude was seen to yield significant improvements; however, small differences still existed, which could be caused by transport limitations for Pb^{2+} ions, a factor not considered in this study. Controlled experiments, where the cell specific parameters (electrode thickness, porosity, surface area, etc.) are known, would provide a means of extracting the exchange current density and the change in the surface area with SOC, by utilizing the mathematical model developed in this paper.

Acknowledgments

The authors gratefully acknowledge financial support from the Department of Transportation Advanced Vehicle Program under cooperative agreement no. DTRS56-99-T-0016. Mr. Russ Owens is acknowledged for performing the experiments.

The Pennsylvania State University assisted in meeting the publication costs of this article.

List of Symbols

a_j	specific surface area per unit volume for reaction j, cm^2/cm^3
$a_{max,j}$	maximum specific surface area per unit volume of reaction, cm^2/cm^3
EUC	electrode utilization coefficient
C	specific capacitance, F/cm^2
c^{H+}	concentration of acid, mol/cm^3
c^{H+}_{ref}	reference acid concentration, mol/cm^3
$c^{O_2}_e$	concentration of oxygen in the electrolyte, mol/cm^3
$c^{O_2}_{e,ref}$	reference concentration of oxygen in the electrolyte, mol/cm^3
D_{H+}	diffusion coefficient of acid, cm^2/s
F	Faraday's constant, 96,487 A s/equiv
i_o	exchange current density, A/cm^2
$i_{oj,ref}$	exchange current density for reaction j at reference conditions, A/cm^2
i_{nj}	transfer current density for reaction j, A/cm^2
R	universal gas constant, 8.3143 J/mol K
T	temperature, K
t	time, s
t^0_+	transference number of H^+ relative to the solvent
U_j	OCP for reaction j, V

Greek

α_{aj}	anodic transfer coefficient for reaction j
α_{cj}	cathodic transfer coefficient for reaction j
ϕ_e	potential in the electrolyte, V
ϕ_s	potential in the solid matrix, V
γ_j, δ_j	exponent for the concentration dependence of the exchange current density
η_j	overpotential for reaction j, V
κ^{eff}	effective ionic conductivity, $\Omega^{-1}\ cm^{-1}$
σ^{eff}	effective electronic conductivity, $\Omega^{-1}\ cm^{-1}$
τ_{Rct}	time constant of a charge-transfer process
τ_{MT}	time constant for a mass-transfer process
τ_{ohmic}	time constant for an ohmic process
ξ	morphology correction factor

Subscripts

2	PbO_2 reaction
3	Pb reaction
4	oxygen evolution reaction
5	hydrogen evolution reaction
6	oxygen reduction reaction
e	electrolyte phase
dl	double layer
s	solid phase

References

1. *Electric Vehicle Battery Test Procedures Manual*, United States Advanced Battery Consortium (USABC), http://www.uscar.org/USABC/usabcmanual.pdf
2. S. Atlung and B. Zachau-Christiansen, *J. Power Sources*, **52**, 201 (1994).
3. R. F. Nelson, E. D. Sexton, J. B. Olson, M. Keyser, and A. Pesaran, *J. Power Sources*, **88**, 44 (2000).
4. S. C. Kim and W. H. Hong, *J. Power Sources*, **89**, 93 (2000).
5. W. Tiedemann and J. Newman, in *Battery Design and Optimization*, S. Gross, Editor, PV 79-1, p. 32, The Electrochemical Society Proceedings Series, Princeton, NJ (1979).
6. W. G. Sunu, in *Electrochemical Cell Design*, R. E. White, Editor, p. 357, Plenum Press, New York (1984).
7. T. V. Nguyen and R. E. White, *Electrochim. Acta*, **38**, 935 (1993).
8. D. M. Bernardi and M. K. Carpenter, *J. Electrochem. Soc.*, **142**, 2631 (1995).
9. J. Newman and W. Tiedemann, *J. Electrochem. Soc.*, **144**, 3081 (1997).
10. W. B. Gu, C. Y. Wang, and B. Y. Liaw, *J. Electrochem. Soc.*, **144**, 2053 (1997).
11. W. B. Gu, C. Y. Wang, and B. Y. Liaw, *J. Power Sources*, **75**, 154 (1998).
12. W. J. Wruck, R. M. Machado, and T. W. Chapman, *J. Power Sources*, **134**, 539 (1987).
13. J. Newman, *J. Electrochem. Soc.*, **117**, 507 (1970).
14. J. O'M. Bockris, Z. Nagy, and A. Damjanovic, *J. Electrochem. Soc.*, **119**, 285 (1972).
15. B. Paxton and J. Newman, *J. Electrochem. Soc.*, **144**, 3818 (1997).
16. I. J. Ong and J. Newman, *J. Electrochem. Soc.*, **146**, 4360 (1999).
17. M. Doyle, J. Meyers, and J. Newman, *J. Electrochem. Soc.*, **147**, 99 (2000).
18. C. Lin, J. A. Ritter, B. N. Popov, and R. E. White, *J. Electrochem. Soc.*, **146**, 3168 (1999).
19. P. C. Milner, *J. Electrochem. Soc.*, **107**, 343 (1960).
20. C. Lagergren, G. Lindgergh, and D. Simonsson, *J. Electrochem. Soc.*, **142**, 787 (1995).
21. H. Bode, *Lead-Acid Batteries*, John Wiley and Sons, New York (1977).
22. W. B. Gu, G. Q. Wang, and C. Y. Wang, *J. Power Sources*, **108**, 174 (2002).
23. J. Newman, *Electrochemical Systems*, Prentice Hall, Inc., Eaglewood Cliffs, NJ (1973).
24. R. E. Meredith and C. W. Tobais, *Conduction in Heterogeneous Systems*, *Advances in Electrochemistry and Electrochemical Engineering*, Vol. 2, C. W. Tobias, Editor, Interscience Publishers, New York (1962).
25. S. V. Patankar, *Numerical Heat Transfer and Fluid Flow, Hemisphere*, Washington, DC (1980).
26. V. Srinivasan and J. W. Weidner, *J. Electrochem. Soc.*, **146**, 1650 (1999).
27. F. A. Posey and T. Morozumi, *J. Electrochem. Soc.*, **113**, 176 (1966).
28. R. M. LaFollette and D. N. Bennion, *J. Electrochem. Soc.*, **137**, 3693 (1990).
29. Y. Guo, R. Groiss, H. Doring, and J. Garche, *J. Electrochem. Soc.*, **146**, 3949 (1999).
30. J. P. Carr and N. A. Hampson, *J. Electrochem. Soc.*, **72**, 679 (1972).
31. I. A. Aguf, *Sov. Electrochem.*, **4**, 1022 (1968).